Available online at www.sciencedirect.com
SCIENCE DIRECT®
Physics of the Earth and Planetary Interiors 153 (2005) 32–48
PHYSICS OF THE EARTH AND PLANETARY INTERIORS
www.elsevier.com/locate/pepi

Deformation of a partially molten D″ layer by small-scale convection and the resulting seismic anisotropy and ultralow velocity zone

Tatsuto Okamoto[a], Ikuro Sumita[b,*], Tomoeki Nakakuki[c], Shigeo Yoshida[a]

[a] *Department of Earth and Planetary Sciences, Nagoya University, 464-8602 Nagoya, Japan*
[b] *Department of Earth Sciences, Faculty of Science, Kanazawa University, Kakuma, Kanazawa 920-1192, Japan*
[c] *Department of Earth and Planetary Systems Science, Hiroshima University, 739-8526 Hiroshima, Japan*

Received 10 November 2004; accepted 28 March 2005

Abstract

Partially molten regions in the lowermost mantle have been inferred to exist by the discovery of the ultralow velocity zone (ULVZ). We consider a small-scale stagnant-lid convection in the D″ layer, following [Solomatov, V.S., Moresi, L.N., 2002. Small-scale convection in the D″ layer. J. Geophys. Res., 107, doi:10.1029/2000JB000063.], to investigate the relationship between partial melt and seismic anisotropies often found in the D″ layer. Such convection can bring melts in the D″ layer from the ULVZ, deform the melt inclusions, and accordingly would profoundly affect seismic structures including anisotropies. We therefore calculate the deformation history of partially molten regions at the base of the D″ layer which is heated from below, using a 2D model with a strongly temperature dependent viscosity. An initially isotropic partial melt is strongly deformed by the viscous stress caused by thermal convection, and becomes anisotropic by shape preferred orientation (SPO) of melt inclusions, whose aspect ratios are of the order of 10^1 to 10^2 at the base of the plume and become as large as 10^3 to 10^4 in the plume head. We calculate the effective elastic constants for such anisotropic media which contain deformed melt inclusions, and obtain the seismic velocity for a horizontal ray path. We find that the horizontally averaged velocity profile can be correlated with convective patterns. If melting occurs not only in the ULVZ but extends to the top of hot regions of the D″ layer, the vertical seismic profile consists of three layers corresponding to the base, conduit and head of a rising plume. The lowermost layer, which corresponds to the ULVZ, becomes strongly anisotropic with $V_{SH} > V_{SV}$. The deformation and alignment of the melt, rather than the melting itself, is primarily responsible for reducing the seismic velocity. On the other hand, in the conduit, the anisotropy is of $V_{SV} > V_{SH}$ type because of vertical alignment. In the plume head, the anisotropy is of $V_{SH} > V_{SV}$ type with a magnitude of about 2%. We discuss how shear wave anisotropy may be used to infer the temporal evolution of the D″ layer.

Keywords: D″ layer; Partial melt; Deformation; Plumes; Ultralow velocity zone; Seismic anisotropy

1. Introduction

The Earth's core-mantle boundary (CMB) region, is the most distinct chemical and thermal boundary layer in the Earth's interior and has been the focus of much interdisciplinary research in the recent years (Lay et al., 1998a; Duffy, 2004).

Seismological observations have shown that the D″ region, the lowermost part of the mantle with an average thickness of about 200 km, has features which largely deviates from the spherically symmetric standard Earth model PREM (Dziewonski and Anderson, 1981). This region is characterized by a small, in some cases negative, vertical velocity gradient and often a discontin-

* Corresponding author. Tel.: +81 76 264 6518; fax: +81 76 264 6545.
E-mail address: sumita@hakusan.s.kanazawa-u.ac.jp (I. Sumita)

0031-9201/$ – see front matter © 2005 Published by Elsevier B.V.
doi:10.1016/j.pepi.2005.03.018

uous velocity jump at the top. A large lateral heterogeneity of about 1.2% and 4% exists for P- and S-wave, respectively. An ultralow velocity zone (ULVZ) at the base has been observed at several locations, and has been attributed to partial melting (Williams and Garnero, 1996; Lay et al., 2004). A shear wave anisotropy of both $V_{SH} > V_{SV}$ and $V_{SH} < V_{SV}$ types has also been observed (see (Garnero, 2000) for a review). Here V_{SH} and V_{SV} are the SH and SV-wave velocities, respectively. Two explanations are given for the origin of anisotropy (see (Kendall and Silver, 1998; Karato, 1998; Lay et al., 1998b; Kendall, 2000) for a review). One is lattice preferred orientation (LPO) of lower mantle minerals, where anisotropic minerals are aligned by dislocation creep. The most promising candidate for producing such anisotropy is the recently discovered post-perovskite phase which transforms from perovskite at pressures corresponding to the depth of D″ discontinuity (Murakami et al., 2004; Oganov and Ono, 2004). From first principles calculations, Iitaka et al. (2004) and Oganov and Ono (2004) found that it has sufficient seismic anisotropy to explain the observed 3% in the circum-pacific region of the D″ layer, if the b-axis aligns in the vertical direction. The other is shape preferred orientation (SPO) where partial melt or chemical heterogeneity forms sheets or laminae by deformation processes. Deformed melt is very efficient in producing a large anisotropy (Kendall and Silver, 1998), and can become an important candidate of anisotropy when melting occurs, and when the stress is too small to produce dislocation creep. We pursue the SPO hypothesis in this paper.

In order to explain the origin of these seismic observations, a number of dynamical modelling of the D″ layer has been made. Christensen (1984) and Olson et al. (1987) calculated the thermal instability and plume generation in the lowermost mantle heated from below, using a fluid with a strongly temperature dependent viscosity. They found that convection starts as small-scale cells beneath a highly viscous stagnant lid and noted that plumes coalesce as they ascend upwards. In the calculation by Olson et al. (1987) the envelope of the plume heads formed a bumpy interface and they proposed this as a candidate for the cause of seismic scattering in the D″ layer. Solomatov (1995) next showed that for a fluid with strongly temperature dependent viscosity three convective regimes are possible with increasing viscosity contrast: a small viscosity contrast regime, a transient regime and a stagnant-lid regime. A stagnant-lid regime occurs for a viscosity contrast exceeding four orders of magnitude. In recent years, more complex calculations have been made. Thompson and Tackley (1998) calculated plume formation in a compressible mantle for a viscosity contrast of up to 2×10^4 and showed that the small-scale convection eventually develops into megaplumes which rise rapidly into the highly viscous overlying mantle. Schott et al. (2002) addressed the issue of the mixing and entrainment of a D″ layer which is less viscous and denser than the ambient mantle. They showed the difficulty of large-scale entrainment, but suggested that the entrainment of small-scale (10–100 km) structures could explain observed 'non-decaying' power spectrum of scattered seismic energy attributed to heterogeneity (Cormier, 2000).

Solomatov and Moresi (2002) showed that small-scale convection can account for various seismological characteristics of the D″ layer. Here the small-scale convection begins as a thermal instability within a large-scale boundary layer which eventually becomes unstable and chaotic. Formation of the large-scale thermal boundary layer can be initiated by several causes. One is when a thermal boundary layer has been swept away by plume formation or by a large-scale flow of the mantle convection. Another is when a subducted slab reaches the CMB and spreads horizontally along the CMB. Such slabs may also be advected by the convective flow towards the upwelling region. In both cases described above, a hot CMB comes in contact with a cold mantle, and a huge viscosity contrast develops.

The dynamical process for the formation of seismic anisotropy has been studied by McNamara et al. (2001, 2002, 2003), who calculated the stress and strain field in the D″ layer caused by a subducting slab. They showed that the resulting high stress may cause the dislocation creep to occur at the downwelling region of the lowermost mantle, causing LPO there. They also found that in the regions of upwelling, the magnitude of stress is too low to cause dislocation creep, and suggested that the origin of anisotropy there may be different. This is consistent with some seismological studies which indicated that SPO in the vicinity of upwelling region in the form of horizontal lamellae best explains anisotropy beneath central America (e.g., Kendall and Silver (1996)) and central Pacific (e.g., Russell et al. (1998), Fouch et al. (2001)). Note that these are also the regions where ULVZ is observed (Lay et al., 2004). However, the model of horizontal lamellae may be too simplistic. Garnero et al. (2004) recently found evidence of azimuthal anisotropy beneath central America, which they interpret as due to inclined lamellae.

A majority of the previous dynamical modelling studies have shown qualitatively that the observed seismic

structure of the D″layer is dynamic in origin. A quantitative approach on relating dynamics with seismology was made by Sidorin and Gurnis (1998), Sidorin et al. (1998, 1999). Here, they computed seismic velocity anomalies and synthetic waveforms for waves travelling through their global numerical models of mantle convection. They showed that the shear waves computed for a model assuming a thermal slab interacting with a phase transition best correlate with the global distribution of the observed D″ triplication. However, there have been no attempts to calculate the seismic anomalies and shear wave anisotropy of waves propagating through the D″ layer which includes largely deformed melt inclusions.

In this paper, we extend the model of Solomatov and Moresi (2002) and calculate how melt pockets are deformed in the upwelling region of the small-scale convection and how they affect seismic velocities and anisotropy. For simplicity, and to consider the effect of partial melting only, we assume that the solid is isotropic and that the melt is neutrally buoyant. With these assumptions, we study how initially isotropic melt pockets are deformed by the viscous stress resulting from small-scale convection. As a partially molten region deforms, it becomes anisotropic due to disk-shaped melt inclusions. As a consequence, the seismic wave velocity anomaly and anisotropy of this layer evolve with time. We calculate the seismic velocity using the elastic constants obtained from an effective medium theory, and study how the dynamics and the seismic structure are related. We find that the model simulates seismically detectable shear wave anisotropy at the base of the plumes, consistent with the observed splitting of $V_{SH} > V_{SV}$. Furthermore, it predicts vertical variations in anisotropy: $V_{SV} > V_{SH}$ in the conduit and $V_{SH} > V_{SV}$ in the plume head. Using the simulated results, we show how seismology may be used to constrain the temporal evolution of the growing D″ layer.

2. Numerical model

In this section, we explain our numerical method. We first explain the convection calculation in Sections 2.1 and 2.2. We then describe the methods to calculate the deformation of melt inclusions in Section 2.3 and the seismic velocity decrement and anisotropy of a medium including melt inclusions in Section 2.4 Note that our model has many simplifications that we shall discuss. Our model is intended to serve as a starting point to making more realistic model of the deformation of partial melt in the D″ layer.

2.1. Governing equations for calculating thermal convection

We carry out a two-dimensional calculation of thermal convection which starts by a sudden increase in the bottom temperature. The whole region is initially isothermal, and then the temperature at the bottom boundary (CMB) is raised in a stepwise manner at $t = 0$ as in Solomatov and Moresi (2002). The calculated region is a rectangular box with 500 km in height and 1500 km in width. The height is chosen so that the top boundary does not affect our results during the 200 Myr period we simulate. Larger heights require much longer computational time, and we confirm that changing the height to 1500 km does not affect the results. The width is chosen so that the lateral boundaries do not affect the development of thermal instability. The validity of two-dimensionality is discussed later in Section 4.4.

We assume an infinite Prandtl number, incompressible Boussinesq fluid. Under the Boussinesq approximation, the mass conservation equation is given by

$$\nabla \cdot \vec{V} = 0, \tag{1}$$

where $\vec{V}$ is the velocity. For infinite Prandtl number, the momentum conservation equation is written as

$$0 = -\nabla P + \nabla \cdot [\eta(\nabla \vec{V} + (\nabla \vec{V})^T)] - \rho^* \alpha \vec{g} \delta T, \tag{2}$$

where P is the pressure, η is the viscosity, α is the thermal expansion coefficient, ρ^* is the reference density, $\vec{g}$ is the gravitational acceleration and δT is the temperature difference from the reference temperature T^*, which we take to be 2500 K. We introduce a stream function Ψ defined as

$$\vec{V} = \left(\frac{\partial \Psi}{\partial z}, -\frac{\partial \Psi}{\partial x} \right), \tag{3}$$

where x is the horizontal coordinate and z is the vertical coordinate with positive upward direction. We rewrite the momentum conservation equation by operating $\nabla \times$ to form a generalized biharmonic equation (Schubert et al., 2001)

$$\left(\frac{\partial^2}{\partial z^2} - \frac{\partial^2}{\partial x^2} \right) \left[\eta \left(\frac{\partial^2 \Psi}{\partial z^2} - \frac{\partial^2 \Psi}{\partial x^2} \right) \right] + 4 \frac{\partial^2}{\partial x \partial z} \left(\eta \frac{\partial^2 \Psi}{\partial x \partial z} \right) = \rho^* \alpha g \frac{\partial T}{\partial x}. \tag{4}$$

The energy conservation equation is

$$\frac{\partial T}{\partial t} + \vec{V} \cdot \nabla T = \kappa \nabla^2 T, \tag{5}$$

where κ is the thermal diffusivity. We ignore internal heat source and heating by viscous dissipation because

Table 1
Fixed parameters

Parameter	Value	Reference
Thermal expansivity: α (K^{-1})	1.0×10^{-5}	Chopelas and Boehler (1989)
Heat capacity: C_p (J/kg K)	1.2×10^3	Navrotsky (1995)
Activation energy : E (kJ/mol)	500	Yamazaki and Karato (2001)
Reference viscosity: η^* (Pa s)	10^{22}	ibid, Lambeck et al. (1990)
Thermal conductivity: k (W/m K)	6.0	Hofmeister (1999)
Density: ρ^* (kg/m^3)	5.0×10^3	Dziewonski and Anderson (1981)
Liquidus temperature:T_L (K)	5500	*
Solidus temperature: T_S (K)	3750	*
Reference temperature:T^* (K)	2500	
Gravitational acceleration: g (m/s^2)	10	

* See text for the derivation of these estimates.

the calculation times are short enough for the internal heatings to take effect. The latent heat on melting is also neglected, whose effects are evaluated in Section 4.5. The equation of state is expressed as

$$\rho = \rho^*(1 - \alpha\delta T), \tag{6}$$

where ρ is the density. We assume an Arrhenius type temperature dependent viscosity given by

$$\eta = \eta^* \exp\left[\frac{E}{R}\left(\frac{1}{T} - \frac{1}{T^*}\right)\right], \tag{7}$$

where η^* is the reference viscosity, E is the activation energy, R is the gas constant, T^* is the reference temperature. The list of parameters are given in Table 1.

Velocity boundary conditions are impermeable and shear stress free at all the boundaries. Thermal boundary conditions are isothermal at the bottom (T_b) and at the top (T_u) and insulating at the sides. We assume a bottom temperature $T_b = 4000$ K, which is the estimate of core temperature at the CMB by Boehler (2000). We have made calculations for several top temperatures, but we primarily describe the results for the case $T_u = 2200$ K (temperature drop across the D″layer = 1800 K) which is an approximate temperature of a cold subducting slab. In this case the resulting viscosity contrast between the top and the bottom boundaries becomes 2×10^5. We will briefly explain the results for other top temperatures T_u in Sections 3.4 and 4.3.

The only one non-dimensional parameter in this problem is the Frank-Kamenetskii parameter, defined as

$$\gamma = \frac{E}{RT_b}\frac{T_b - T_u}{T_b} \tag{8}$$

(Solomatov, 1995; Solomatov and Moresi, 2002) which controls the viscosity contrast. For $T_u = 2200\,K$, the Frank-Kamenetskii parameter is about 7. According to Stengel et al. (1982), who investigated the onset of convection for the viscosity depending exponentially on the temperature, $\gamma = 8$ marks the boundary between the whole-layer convection mode and the stagnant-lid convection mode. Our parameter value of 7 thus signifies that our calculation is in the whole-layer convection regime. However, the difference in the temperature dependence of the viscosity between Stengel et al.'s (1982)and ours makes the assignment difficult. It may be more appropriate to state that our calculation is in the transition region between the stagnant-lid and whole-layer modes.

2.2. Numerical method for convection calculations

We use a finite difference method based on the control volume scheme for spatial discretization. Variables are defined on a uniform staggered grid. Eq. (4) is solved by a modified Cholesky decomposition method to avoid numerical instabilities caused by large viscosity variation (Nakakuki et al., 1994). We use a partially upwind scheme to calculate the advection term in the energy equation (Clauser and Kiesnar, 1987). A semi-implicit Euler method is used for time-marching with a variable time step. The Courant number $c_{i,j}$ defined at each grid point (i, j) as

$$c_{i,j} = \frac{(|V_x^{i,j}| + |V_z^{i,j}|)\delta t}{\delta l} \tag{9}$$

is used to determine the time step δt. Here, $V_x^{i,j}$ and $V_z^{i,j}$ are the x and z components of the velocity, respectively, at the grid point $(i.j)$, and δl is the mesh size. The time step δt is determined so that the Courant number is less than 0.2. Since the time step becomes too large at the beginning of the calculation with the condition above, we set the maximum time step to be 10^5 years.

The mesh size is 2.5 km, so that the number of meshes is 600 in the x direction and 200 in the z direction for the calculated area of 1500 km × 500 km. We check whether the mesh size warrants sufficient precision. We use mesh sizes of 5, 2.5, 1.25 0.625 km to calculate the heat flow at the bottom. We find that the error is 10% for 5 km mesh,

2–3% for 2.5 km mesh and less than 1% for 1.25 km mesh. We conclude that the vertical mesh size of 2.5 km is sufficient to resolve the thermal boundary layer and use it for our calculations.

Initially, a random lateral thermal perturbation of less than 1% of the temperature difference between the top and bottom is given at the lowermost meshes (i.e., in a height of 2.5 km) to trigger thermal instability. We check the effect of initial temperature perturbation on the onset time of instability as follows. When the perturbation is distributed in the bottom layer with a height of 50 km, we find that the onset time of instability becomes approximately 5 Myr earlier, corresponding to a 7–8% error. When the amplitude of the initial perturbation is 10 times larger (i.e., 10% of the temperature difference between the top and bottom), the onset of instability also becomes earlier by 5 Myr.

2.3. Deformation calculations

Melt pockets, which give rise to seismic heterogeneities and anisotropies, behave as passive tracers in our calculation. We assume that the melting (and solidification) occurs when the tracer crosses the solidus isotherm. Then these tracers deform in the form of strain ellipses and are advected by the solid mantle flow. For simplicity, the melt density is assumed to be equal to the solid matrix, and liquid and solid do not separate gravitationally.

For our calculations, we assume that the melt fraction ϕ is proportional to the temperature above solidus as

$$\phi(T) = \frac{T - T_S}{T_L - T_S}, \tag{10}$$

where T_S and T_L are the solidus and liquidus temperatures, respectively. Zerr et al. (1998) estimated the solidus at the CMB as 4300 K. Considering the proximity of this temperature and that of the outer core at the CMB (4000 ± 200 K) (Boehler, 1996), they concluded that partial melting is possible in the lowermost mantle. If we take these values as correct, partial melting is impossible unless chemical heterogeneities are taken into account, because the core temperature at the CMB should be uniform due to the fluid motion in the outer core. Considering the uncertainties of these temperatures, we have tried calculations for several values of the solidus temperature, and choose the value $T_S = 3750$ K, for which the resulting seismic structure is most interesting. The effect of changing the the solidus temperature is briefly discussed in Section 4.3. For the liquidus temperature we use the estimated melting temperature of $(Mg,Fe)SiO_3$ in Boehler (2000), and take $T_L = 5500$ K. For the above choices of the liquidus and solidus, the maximum melt fraction reaches approximately 14% at the bottom ($T = 4000$ K). These adopted melting temperatures are uncertain, but since the goal of our paper is to show that this mechanism of producing anisotropies is possible when partial melt exists, we mainly show the results for just one choice of the temperatures. It is also to be noted that the differences of the melting temperatures and the CMB temperature are more important than their absolute values.

Tracers in the form of the strain ellipse are used to describe the macroscopic deformation of partially molten aggregate. Initially, we uniformly distribute the tracers, four per mesh (a total of 4.8×10^5 tracers), and let them passively advected by the flow. They are circular when they are below solidus. When they cross the solidus, we start calculating their deformation. When the tracer reenters the completely solid region, its shape is assumed to become circular again. The shapes of the strain ellipses are used to estimate the degree of seismic anisotropy as we explain in Section 2.4. We track the tracers by fourth order Runge-Kutta method. The deformation is calculated by integrating the velocity gradient tensor in a Lagrangian way to obtain its finite strain tensor (McKenzie, 1979). We use the finite strain to obtain the aspect ratio and the direction of the major axis of the elliptical tracer.

The deformation calculation in this paper is simplified and we discuss below the plausibility and caveats of these simplications.

First, we assumed neutrally buoyancy for simplicity. We note, however that Lay et al. (2004) showed that neutral buoyancy is possible, considering the small volume change on melting at high pressures, difference in thermal expansivity between the solid and melt, and possible iron partitioning.

Second, we assumed an elliptical shape for the melt. In reality, melt could form interconnected channels around the grain boundaries. An elliptical shape represents a macroscopic anisotropy of the partially molten aggregate, and does not necessarily imply that the melt itself is elliptical. We argue that this shape is sufficient for calculating seismic velocities because the qualitative effect to the long-period seismic waves would not be sensitive to the details of the melt topology.

Third, we assume that the deformed partial melt does not texturally equilibrate to become isotropic again by surface tension. If the melt were texturally equilibrated, there would be no anisotropy when there is no preferred orientation of solid grains. The condition for textural equilibrium to occur is that the surface tension overwhelms the viscous stress. The viscous stress τ is at least

of the order of 10^5 Pa (see Fig. 6). Using surface tension coefficient of $\sigma \simeq 0.5$ N/m (Cooper and Kohlstedt, 1982), the ratio of viscous stress to surface tension is

$$\frac{\tau D}{\sigma} \simeq 2 \times 10^3 \left(\frac{D}{10^{-2}\mathrm{m}} \right), \tag{11}$$

where D is a typical grain size. This value is much larger than unity for plausible grain sizes, showing that viscous stresses dominate.

Fourth, we assumed that the additional melting and/or freezing would not modify the aspect ratio. In reality, additional melting would reduce the aspect ratio, and vice versa for freezing, since melting and/or freezing depends only on the local condition and does not depend on the shape of melt pockets. This effect would result in the overestimate of the aspect ratio when the temperature increases, and the underestimate when the temperature decreases. Note that there are at least two ways of increasing melt volume; melting an existing pocket and generating a new melt pocket. To avoid introducing further complexity, this effect was neglected.

Finally, we compare with laboratory experiments of deformation of partially molten olivine and basalt (Zimmerman et al., 1999; Holtzman et al., 2003), which were done at higher stress but smaller total strain compared to the calculations in this paper. These experiments showed that melt sheets tend to align parallel to the principal stress axis. However, this type of melt alignment would not occur under low stress levels in the D″ layer (Zhang et al., 1995) as Karato (1998) argued. We consider that passive deformation would become important when total strain becomes much larger than unity which is the case in our calculations.

2.4. Seismic velocity of an effective medium

We calculate seismic properties of a medium with melt inclusions deformed as described in Section 2.3. We first calculate effective elastic constants. Using these elastic constants, we calculate the seismic velocities and then obtain horizontally averaged seismic velocities.

We calculate the effective elastic constants of a deformed partial melt by the method of Nishizawa and Yoshino (2001), which is based on the theories of Eshelby (1957) and Nishizawa (1982). In this method, elastic constants are calculated iteratively by incrementally increasing the melt fraction. Similar calculations were carried out by Singh et al. (2000) and Taylor and Singh (2002) for different applications. The uniform strain condition, which corresponds to the Voigt average giving the upper bounds of elastic constants, is used to calculate the elastic constants. We assume a spheroidal melt inclusion in an isotropic matrix, so the elastic constants become functions of the melt fraction and the aspect ratio of the melt inclusion. In a 2D flow, as assumed in this paper, the flow is uniform in the third direction, and a spheroidal melt would become oblate, i.e., flat disk with the aspect ratio >1, whose symmetrical axis lies in the 2D plane of the flow. For the elastic constants of the isotropic solid matrix, we use the PREM value at the lowermost mantle, $K = 655.6$ GPa and $\mu = 293.8$ GPa, and for the melt we use $K = 605$ GPa and $\mu = 0$ GPa (Williams and Garnero, 1996).

We next use these elastic constants to calculate V_P, V_S1, V_S2 from the velocity equation for a hexagonal symmetry (Musgrave, 1970). Here V_P, V_S1 and V_S2 are the phase velocities of the P, S1 and S2 waves, respectively. The S1 wave is polarized in the plane perpendicular to the symmetrical axis of the spheroid (i.e. (0 0 1) plane in hexagonal symmetry). The S2-wave is polarized in the plane parallel to the symmetrical axis of the spheroid (i.e. (0 1 0) plane). For a ray travelling horizontally in the calculated 2D plane, the S1-wave is the SH-wave and the S2-wave is the SV-wave, irrespective of the alignment of spheroidal melt pockets. In Figs. 1–3, we plot V_P, V_S1 and V_S2 as a function of the angle between the symmetry axis of the spheroid and the wave number vector, for a melt fraction of $\phi = 0.05$ and aspect ratios of $\alpha = 1$, 10, 100, 1000. The direction of the wave number vector is approximately the propagation direction when the anisotropy is not very strong. As shown in these figures, for a constant melt fraction, the S-wave velocity dramatically decreases with flattening of the spheroid. Shear wave anisotropy can be evaluated from the difference between the S1 and S2 velocities. When the propagation direction is close to the axis of the flat disk $V_\mathrm{SV} > V_\mathrm{SH}$ and the difference is small. On the other hand, when the propagation direction is perpendicular to the axis of the spheroid, $V_\mathrm{SH} > V_\mathrm{SV}$ and their difference is large. The crossover angle for $V_\mathrm{SV} = V_\mathrm{SH}$ decreases as the melt fraction increases. As a function of aspect ratio, the crossover angle increases with the aspect ratio when the aspect ratio is less than about 50. Above aspect ratio of 50, it decreases slightly, and then becomes approximately independent of aspect ratio. When the melt fraction is 0.1, this asymptotic angle is about 58°.

Using these results, we calculate the horizontally averaged seismic velocity $\bar{V}(z)$ at each depth as follows. For each tracer, we use the angle between the axis of the spheroid from the horizontal ray path, the melt fraction and the aspect ratio of the melt to calculate the effective seismic velocity. The horizontal average is obtained by

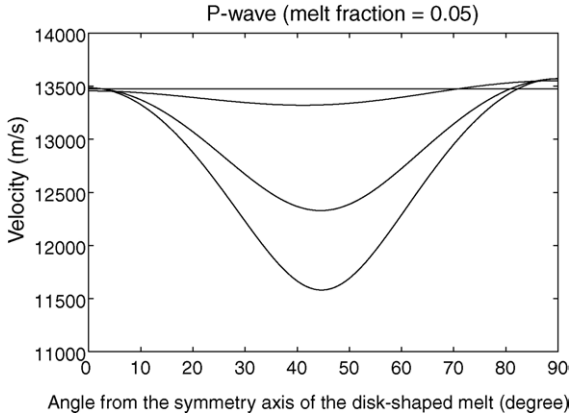

Fig. 1. P-wave velocity as a function of the angle between the wavenumber vector and the symmetry axis of the spheroidal disk melt inclusion for a melt fraction of $\phi = 0.05$. The lines represent results for aspect ratios of 1, 10, 100 and 1000. The P-wave velocity decreases with aspect ratio.

numerically integrating

$$\frac{L}{\overline{V}(z)} = \int_0^L \frac{\mathrm{d}x}{V(x,z)}, \tag{12}$$

where L is the width of the calculation region. Here we use the phase velocity for V instead of the group velocity, although the direction of the group velocity is different from the phase velocity. The use of the phase velocity can be justified by the fact that the projection of the group velocity in the direction of the wave number vector is identical to the phase velocity as

$$\frac{\partial\omega}{\partial\boldsymbol{k}} \cdot \frac{\boldsymbol{k}}{k} = \frac{\omega}{k}. \tag{13}$$

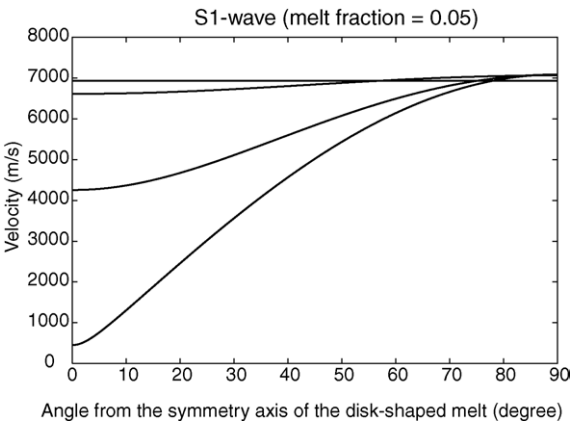

Fig. 2. S1-wave velocity (polarized in (0 0 1) plane) as a function of the angle between the wavenumber vector and the symmetry axis of the spheroidal disk melt inclusion for a melt fraction of $\phi = 0.05$. The lines represent results for aspect ratios of 1, 10, 100 and 1000. The S1-wave velocity decreases with aspect ratio.

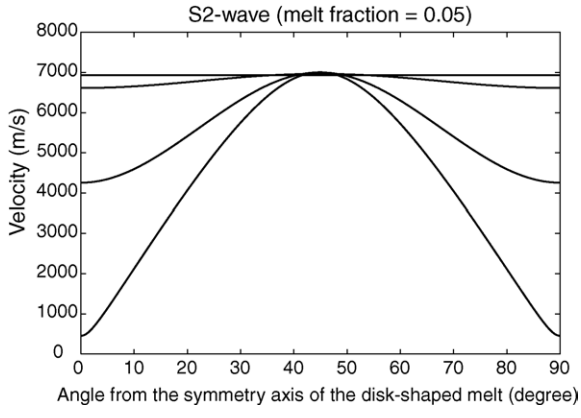

Fig. 3. S2-wave velocity (polarized perpendicular to both S1 polarization and the propagation direction) as a function of the angle between the wavenumber vector and the symmetry axis of the ellipsoidal disk melt inclusion for a melt fraction of $\phi = 0.05$. The lines represent results for aspect ratios of 1, 10, 100 and 1000. The S2-wave velocity decreases with aspect ratio.

This equality holds because the frequency ω is a linear function of the wave number $\boldsymbol{k}$.

3. Results

3.1. Evolution of the D″ thermal instability

Fig. 4 shows the results of the time evolution of the thermal instability in the lowermost mantle. Here the temperature is raised by 1800 K at the base ($T_u = 2200$ K, $T_b = 4000$ K) at $t = 0$. A thermal boundary layer develops from the bottom by thermal diffusion, with a thickness $\sim\sqrt{\pi\kappa t}$, until the onset of small-scale convection at approximately 60 Myr. At 60 Myr, the thickness of the thermal boundary layer is about 80 km. The small-scale convection forms a layer, which we identify with the D″ layer, following Solomatov and Moresi (2002) as explained in Section 1. As convection develops, adjacent plumes coalesce intermittently, and the plumes decrease in number so that the aspect ratio of the convective cells is about 1. The growth rate of the thickness of the convective layer is approximately 1.4 mm/year. Small-scale convection eventually transforms to large-scale instability (not shown in Fig. 4). It indicates that this type of the D″ layer is in a transient state. However, we note that this small-scale convection stage persists even after 200 Myr for the case shown in Fig. 4, and is geologically long. The onset time of instability of 60 Myr can be explained in terms of a simple linear stability theory. If convection starts when a local Rayleigh number reaches a critical value Ra_{cr} (e.g.

(Schubert et al., 2001)), the onset time t_{cr} is given by

$$t_{cr} = \frac{1}{\pi\kappa}\left(\frac{\eta\kappa Ra_{cr}}{\rho^*\alpha g(\Delta T)}\right)^{2/3}. \quad (14)$$

In obtaining this expression, we assume that the whole conductive thermal boundary layer begins to convect since the Frank-Kamenetskii parameter γ is less than 8 (Stengel et al., 1982). The choice of η is a subtle problem for evaluating this onset time. If we interpret Stengel et al.'s (1982)result as indicating that the geometric mean of the viscosities at the upper and lower boundaries is the appropriate choice for η, then $\eta = 5.7 \times 10^{20}$ Pa s. If we interpret Stengel et al.'s (1982)result as indicating that the viscosity at the mean temperature of the upper and lower boundaries is the appropriate choice for η, then $\eta = 9.5 \times 10^{19}$ Pa s. For $Ra_{cr} = 1568$ (Stengel et al., 1982) together with the values in Table 1, we obtain $t_{cr} \approx 100$ Myr for the former choice of η, and $t_{cr} \approx 30$ Myr for the latter choice. Our result of 60 Myr is between these two values.

The onset time of 60 Myr is determined from the time step at which temperature contours transform from conductive profile to laterally heterogeneous convective profile. Although the onset time is not strictly defined, the error is within about ±5 Myr, since the transition to a small-scale convection state is rapid as can be seen later in Figs. 12 and 13.

3.2. Deformation history in the D″ layer

Fig. 5 shows the deformation history of three tracers during the time interval of 165–171 Myr, superimposed on the thermal structure at 171 Myr. Here, the tracers are deformed only when the temperature exceeds the solidus (3750 K). The tracer marked in red is located at the outermost part of the convective cell and shows the largest deformation. The tracers are stretched approximately in the direction of the maximum tension. As a result, the tracers are stretched horizontally within the bottom thermal boundary layer and at the top part of the cell, and vertically in the conduit. Consequently, a three-layer structure of the melt orientation forms. The aspect ratio can be used as a measure of the magnitude of the deformation. From this figure, we find that the deformation is largest in the plume head, and next largest at the base of the plume. The loci of the tracers approximately form a closed loop, indicating that the convective pattern can be well approximated as quasi-stationary Bénard convection. After one circulation of the outermost tracer, the thickness of the convective layer increases by only 20 km. Fig. 6 shows the evolution of the temperature,

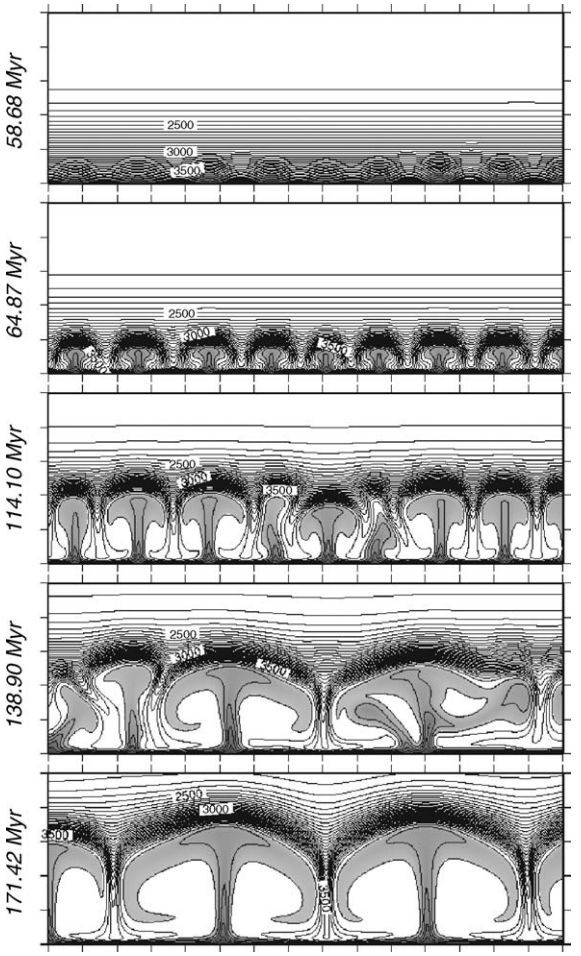

Fig. 4. Evolution of small-scale convection with time. The horizontal and vertical scales are 750 and 250 km, respectively, and is a close up view of the total calculated area of 1500 km × 500 km. The bottom and top temperatures are $T_b = 4000$ K and $T_u = 2200$ K. From the top, each figure corresponds to 64.87, 100.03, 130.14, 149.76 and 171.42 Myr from the beginning of calculation. The contour lines are isotherms, and the numbers on the lines and the corresponding temperatures in K. The dark shade indicates partially molten regions.

stress, strain rate and aspect ratio of the red tracer, whose period of circulation is about 12 Myr. The green tracer, on the other hand, orients vertically at the upper part of the cell. The blue tracer does not experience any deformation because it does not melt. Both the green and blue tracers have circulation periods shorter than that of the red tracer. Upon coalescence of convection cells the tracers take complicated paths and are deformed in a complex manner. We note that the stress level normalized to the shear rigidity is of the order of 10^{-7} and is likely to be in the diffusion creep regime (Frost and Ashby, 1982), making it difficult for LPO to form.

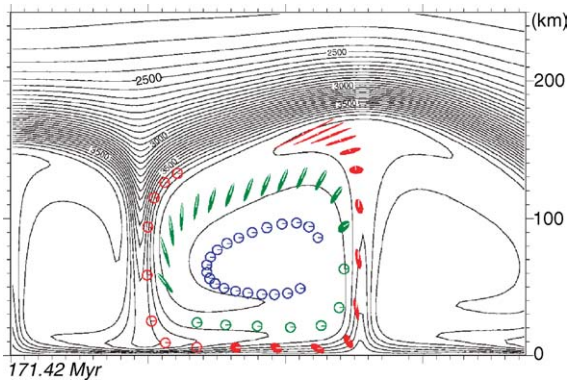

Fig. 5. Evolution of the deformation of melt inclusions indicated by strain ellipses. The horizontal and vertical scales are 375 and 250 km, respectively. The bottom and top temperatures are $T_b = 4000$ K and $T_u = 2200$ K. The contour lines are isotherms (K) at 171.42 Myr. Solid ellipses are melt tracers, whose aspect ratios are drawn in log scale. The trajectory of three tracers from 164.69 to 171.42 Myr are shown in different colors. The filled and open ellipses indicate molten and solid states, respectively. Deformation occurs when the tracer enters the region above the solidus temperature of 3750 K. White reference line in each filled ellipse is directed horizontally rightwards when melting starts, and shows the rotation of each tracer.

Fig. 7 shows a contour plot of the aspect ratio (in the logarithmic scale) of the deformed partial melt. Here an aspect ratio of unity indicates an isotropic partial melt. The plot shows that the aspect ratio is greater than 10^3 in the conduit, and reaches 10^4 in the the uppermost part of the plume head. On the other hand, the aspect ratio takes a minimum value in a region just below the plume head (blue region in Fig. 7). This is because in this region, the principal tension axis changes from vertical to horizontal, and the vertically stretched tracer experiences vertical compression, as can be seen from tracking the red tracer in Fig. 5 (see the sixth and seventh tracers from the uppermost tracer in the plume head).

3.3. Seismic anisotropy in the D'' layer

Fig. 8 shows the directions of the major axes of all tracers above the solidus temperature. They are shown in blue when $V_{SH} > V_{SV}$ and red when $V_{SV} > V_{SH}$ for a seismic ray travelling horizontally in the 2D plane. From the angle of the major axis from the horizontal, we can calculate the corresponding SH and SV velocities for a horizontal ray path, using the results shown in Figs. 2 and 3, and can map the magnitude of shear wave anisotropy $((V_{SH} - V_{SV})/V_{PREM} \times 100)$ as shown in Fig. 9. Here the region with $V_{SH} > V_{SV}$ is shown in blue and the region with $V_{SV} > V_{SH}$ in red. From this figure, we find that three regions with different senses of anisotropy can be defined: (1) $V_{SH} > V_{SV}$ region in the lowermost boundary layer with anisotropies of more than 30%; (2) $V_{SV} > V_{SH}$ region in the conduit with anisotropies of $< 1\%$ and in both sides of the plume head with anisotropies of 0–3%; and (3) $V_{SH} > V_{SV}$ in the upper part of the plume head with anisotropies of up to about 17%. Along the plume axis, tracers rise to the upper thermal boundary layer and are stretched vertically, resulting in $V_{SV} > V_{SH}$ type anisotropy. Slightly off-axis, tracers are strongly stretched horizontally, resulting in $V_{SH} > V_{SV}$ type anisotropy in the plume head (see the red tracer in Fig. 5). Outside the plume head, tracers are stretched vertically, resulting in $V_{SV} > V_{SH}$ type anisotropy (one of such tracers is the green tracer in Fig. 5). The region below the solidus does not contribute to anisotropy. It is not shown and corresponds to the case for the blue tracer in Fig. 5.

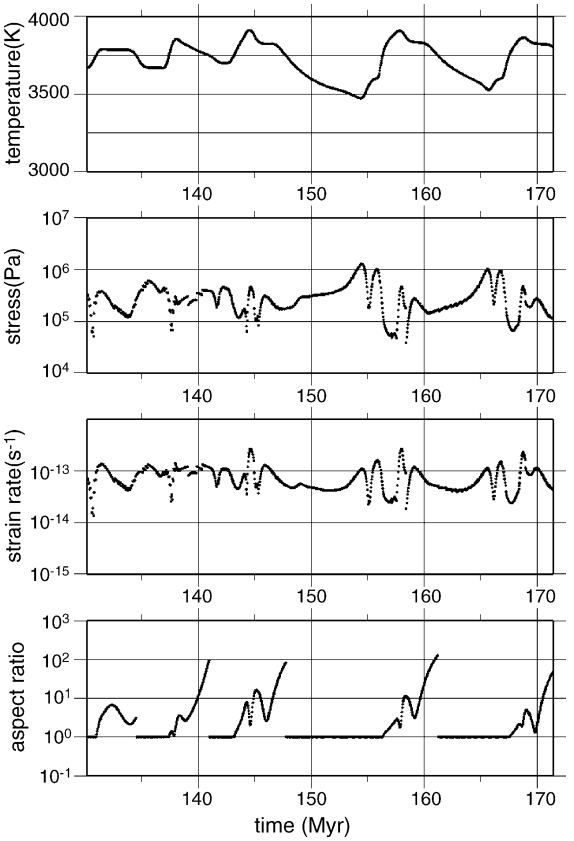

Fig. 6. The time evolution of the temperature, stress, strain rate and aspect ratio for the outermost (red) tracer shown in Fig. 5.

Fig. 10 shows the vertical profile of the horizontally averaged P-wave velocity anomaly. The plot shows that the P-wave is slower than the PREM model by about 0.5% in the plume head, only slightly slower than or comparable to the PREM model in the conduit. In the lowermost thermal boundary layer there is a ULVZ with a

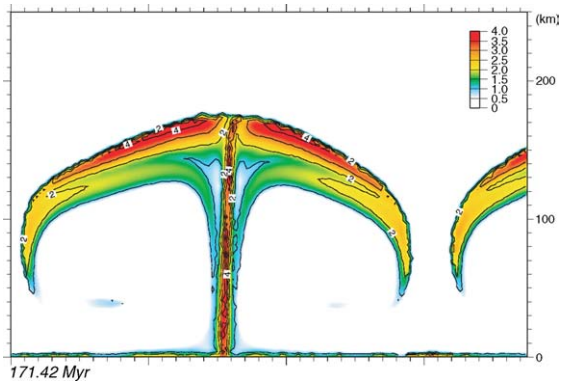

Fig. 7. Aspect ratio of strain ellipses at 171.42 Myr. The horizontal and vertical scales are 375 and 250 km, respectively. The bottom and top temperatures are $T_b = 4000$ K and $T_u = 2200$ K. Numbers are the aspect ratio in log scale.

velocity decrement of 3–4%. The thickness of the ULVZ increases with time: about 5 km at 64.87 Myr to about 10 km at 164.69 Myr. These are also the regions where P-wave velocities are laterally heterogeneous with amplitudes of 0.1–0.2 km/s. Similarly, Fig. 11 shows the vertical profile of the horizontally averaged SH and SV velocity anomalies, along with the degree of anisotropy, $V_{SH} - V_{SV}$ normalized by the PREM S-wave velocity, at 164.69 Myr. The velocity profiles have negative gradients whose steepnesses decrease with time. The layered structure of shear wave anisotropy is evident on the anisotropy profile. Here we find that the SH-wave is faster than the SV-wave by 1–2% in the plume head due to horizontal alignment, whereas vertical alignment in the conduit results in the SV wave faster by 0–1%. Near the base, horizontal alignment gives rise to $V_{SH} > V_{SV}$ type anisotropy of about 1%. In the lowermost 5 km,

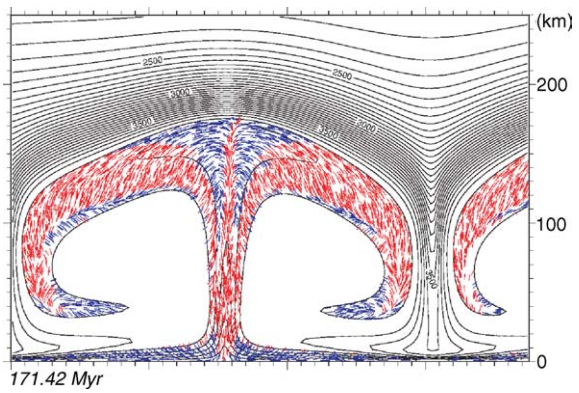

Fig. 8. Major axes of strain ellipses shown in blue for tracers with $V_{SH} > V_{SV}$ and red for those with $V_{SH} < V_{SV}$. The bottom and top temperatures are $T_b = 4000$ K and $T_u = 2200$ K. The horizontal and vertical scales are 375 and 250 km, respectively. Contours are isotherms at 171.42 Myr.

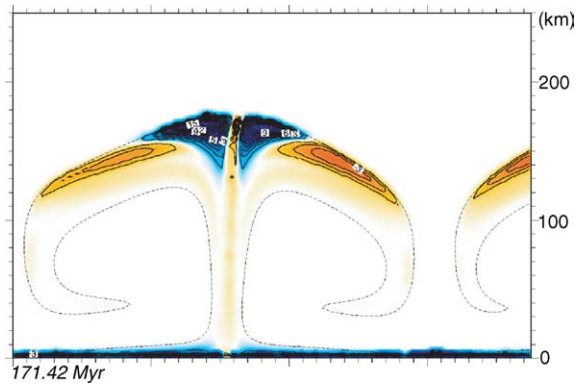

Fig. 9. Contour lines of S-wave anisotropy (%) in the small scale convection for a seismic wave travelling horizontally in the calculated 2D plane. The bottom and top temperatures are $T_b = 4000$ K and $T_u = 2200$ K. The region with $V_{SH} > V_{SV}$ and $V_{SH} < V_{SV}$ are shown in blue and red, respectively. Contours represent the magnitude of anisotropy (%) relative to the PREM model. Dashed line represents the solidus temperature. The horizontal and vertical scales are 375 and 250 km, respectively.

$V_{SH} > V_{SV}$ anisotropy becomes so huge (60–70%) that it is scaled out from this figure. Here, the SV velocity decrement is about 80%, whereas the SH velocity decrement is about 10–20%. This indicates that the contribution of the melt fraction to shear wave velocity decrease is less than that of deformation. The lateral heterogeneity of the shear wave velocity is largest near the CMB, and its amplitude is in the range of 0.5–1.0 km/s.

3.4. Evolution of ULVZ

Figs. 12 and 13 show the time evolution of seismic velocity decrease and shear wave anisotropy in the ULVZ, the lowermost part (0–2.5 and 2.5–5.0 km) of our model, for three different top temperatures: 2200, 2000 and 1500 K. The pattern of time-evolution is similar for these three cases. A faster evolution for larger top temperatures is due to earlier onset of plume instability. We mainly describe the case with $T_u = 2200$ K in the following.

We can define three stages. The first stage is when the melt fraction increases by thickening of the thermal boundary layer. As a result, the P-wave velocity decreases by about 5% and the S-wave velocity decreases by about 12% in the height range of 0–2.5 km above the CMB. Velocity decrement in the height range of 2.5–5.0 km above the CMB is smaller due to less melting. The second stage is when the seismic velocity changes in a stepwise manner by the onset of thermal instability and plume generation. The thermal boundary layer becomes thinner, and the temperature at the lowermost re-

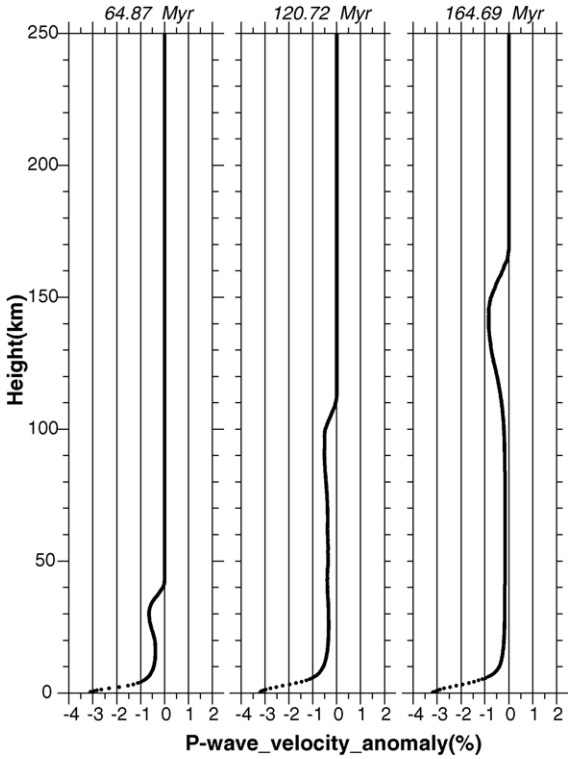

Fig. 10. Evolution of the vertical profiles of the horizontally averaged P-wave velocity anomaly (%) travelling in the calculated 2D plane for 64.87, 120.72, 164.69 Myr from left to right.

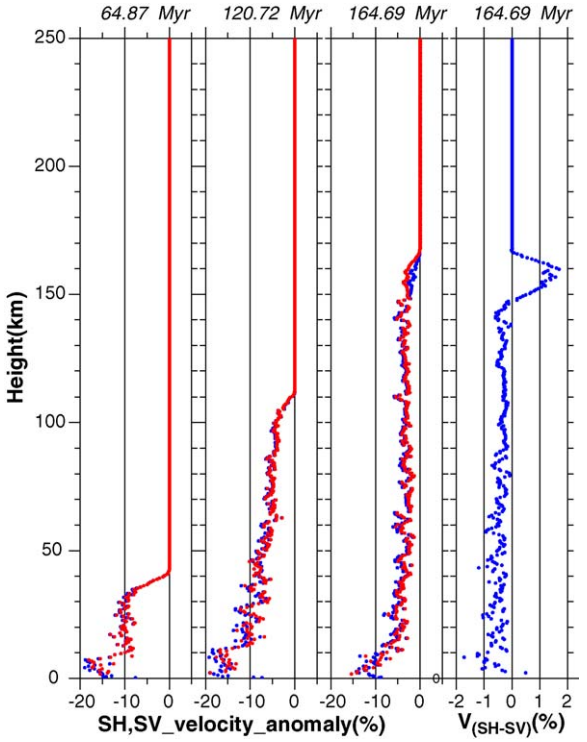

Fig. 11. Evolution of the vertical profile of the horizontally averaged S-wave velocity anomaly (%) after 64.87, 120.72, and 164.69 Myr from left to right. Blue and red dots are SH-wave and SV-wave velocity, respectively. The rightmost profile shows the degree of S-wave anisotropy at 164.69 Myr, expressed as $V_{SH} - V_{SV}$ normalized by the PREM velocity.

gion decreases relative to stage 1. As a consequence, the melt fraction decreases. In Fig. 12, the P-wave velocity increases by about 2%. The SH-wave velocity increases by 4% and then decrease by 9% whereas the SV velocity decreases by about 80% followed by an increase of 10%. These fluctuations arise from deformation and flattening of the partial melt after the onset of instability. The flattening of partial melt to an aspect ratio of 100 strongly affects the SV velocity compared to the SH velocity (see Figs. 2 and 3). This results in a drastic increase of shear wave splitting with the onset of convection. Finally, the third stage is when the P-wave velocity remains approximately constant whereas the SH and SV velocities display irregular fluctuations. These fluctuations are due to coalescence of plumes. Compared to the height range of 0–2.5 km above the CMB, in the height range of 2.5–5.0 km, the SH velocity decrease and the amplitude of the fluctuations are larger and the SV velocity decrease is smaller. This is because most of the deformed melts in the height range of 0–2.5 km align horizontally, whereas the deformed melts in the height range of 2.5–5.0 km are mostly inclined. It follows that the sense of the anisotropy for the height range of 2.5–5.0 km is $V_{SV} > V_{SH}$ with a smaller magnitude of 2–3%.

4. Discussion

4.1. Comparison with seismic observations

A key feature of our results is that it produces a negative shear wave gradient, anisotropy and ULVZ by partial melting only. We note that partial melt is not confined to the ULVZ but exist throughout the D″ layer in our calculations. The ULVZ corresponds to the lower boundary layer of small-scale convection in our model. We now compare our simulations with seismic observations and discuss how we can better constrain the dynamics occurring at the possible partially molten layer at the base of the mantle.

We have found a three-layer anisotropy structure in Section 3.3. Our model predicts a low P-wave velocity and $V_{SH} > V_{SV}$ anisotropy at the plume head where the melt is stretched horizontally. This is consistent with the observation by Thomas et al. (1998) who found a low P-wave velocity sheet of a thickness of 8 km at about 282 km above the CMB, and also with the result of Fouch et al. (2001) who observed a large $V_{SH} > V_{SV}$ anisotropy

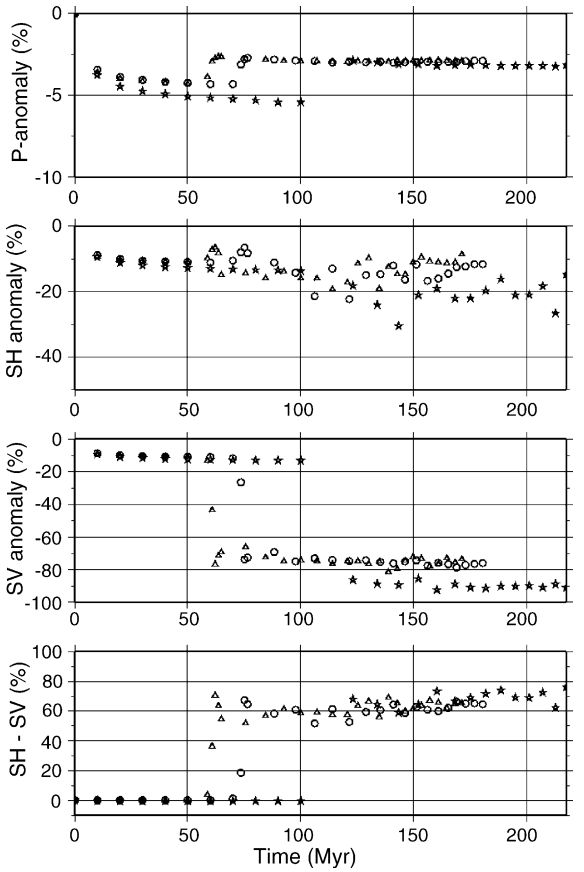

Fig. 12. The evolution of the seismic wave velocity at a height range of 0–2.5 km above the CMB. Three types of symbols represent three runs with different temperatures at the upper boundary (T_u). Triangles, circles and stars indicate the results for $T_u = 2200$, 2000 and 1500 K, respectively. The bottom temperature is 4000 K for all cases.

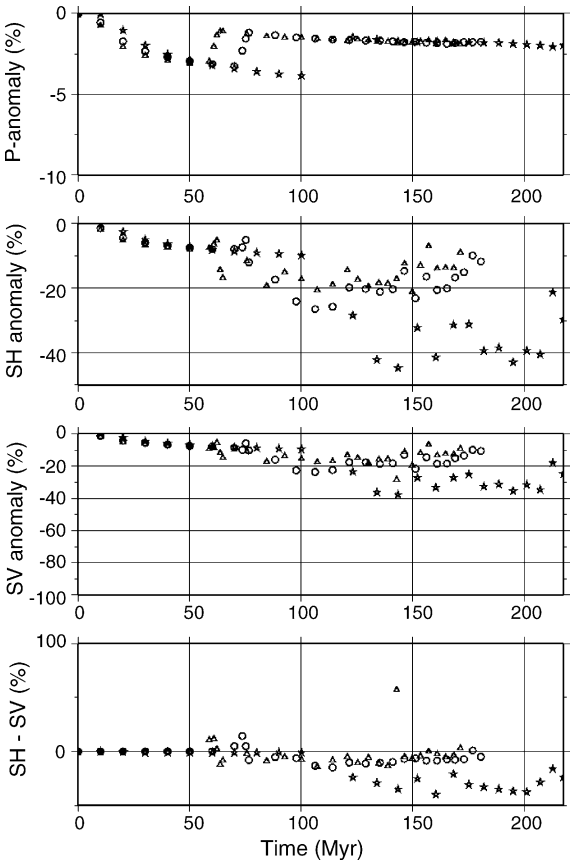

Fig. 13. The evolution of the seismic wave velocity at a height range of 2.5–5 km above CMB. Three symbols represent three runs with different temperatures at the upper boundary (T_u). Triangles, circles and stars indicate the results for $T_u = 2200$, 2000 and 1500 K, respectively. The bottom temperature is 4000 K for all cases.

at about 200 km above the CMB. Our model also predicts a strongly anisotropic SH > SV layer with V_P/V_{SH} ratio of 2 and a huge V_P/V_{SV} ratio of 6–17 at the bottom of the ULVZ (0-2 km), which does not seem to be clearly observed yet or is beyond the detectability.

Seismic observations have reported more $V_{SH} > V_{SV}$ type anisotropy than the $V_{SV} > V_{SH}$ type in the D″ layer. This is also evident from recent global waveform tomography (Panning and Romanowicz, 2004) and is consistent with our result shown in Fig. 11. We obtain large anisotropy of $V_{SH} > V_{SV}$ type near the top and at the base of the D″ layer. On the other hand, the magnitude of $V_{SV} > V_{SH}$ type anisotropy in the mid-D″ layer is small. This results from two causes. One is the large $V_{SH} - V_{SV}$ for a horizontally flattened ellipsoids at the top and the base. The other is that horizontal ray paths pass through these horizontally stretched regions for a longer distance.

Small scale seismic heterogeneities of the D″ layer are of interest in relation to small scale convection. For example, in the region beneath the Pacific, both partial melting (Williams and Garnero, 1996; Revenaugh and Meyer, 1997) and anisotropy of both $V_{SH} > V_{SV}$ and $V_{SV} > V_{SH}$ have been reported (Vinnik et al., 1995; Pulliam and Sen, 1998; Ritsema et al., 1998; Russell et al., 1998, 1999; Fouch et al., 2001). The spatial heterogeneities of these velocity anomalies are highly variable and their length scales are small. Ritsema et al. (1997) found that heterogeneities of 0.5–1% in the shear wave velocity varies in spatial scales of 100–500 km. Russell et al. (1998, 1999) found that the the sense of shear wave anisotropy also changes from $V_{SH} > V_{SV}$ to $V_{SV} > V_{SH}$ by short spatial scales of several 100 km, and suggested that such structure may be formed by shear flow and upwelling of plumes. If the seismologically obtained heterogeneity of several hundred kilometers corresponds to the cell size of small-scale convection, the height of the

convection layer would also be of the order of a hundred kilometers, because the aspect ratio of convective cells is about unity. Our simulations show that such a layer with anisotropies and heterogeneities of similar magnitudes can form in a timescale of about 100 Myr.

4.2. Cases for other ray path geometries

In the simple case discussed in previous sections, the ray path is horizontal within the calculated 2D plane. Here we consider two other geometries as end member cases and describe their qualitative features. For horizontal ray paths perpendicular to convection rolls, S1=SH wave, and S2= SV wave. However, for other ray path geometries, the correspondence of S1, S2 waves to SH, SV waves can become complicated. We note that because our calculations were in 2D, we assume that the alignment is uniform in the third direction.

The first case is where the ray travels vertically in the calculated 2D plane, which corresponds to PcP or ScS waves with small epicentral distances. In this case, the plane of polarization is horizontal for both S1 and S2 waves. When the seismic ray travels through a vertically stretched melt such as along the plume conduit, the plane of polarization for S1-wave is perpendicular to the 2D plane, while that of S2-wave is within the 2D plane. Because the axis of symmetry of the ellipsoids are perpendicular to the ray path, from Figs. 2 and 3, we find that $V_{S1} > V_{S2}$. As a result, shear wave travelling through the conduit will experience large splitting and the wave polarized perpendicular to the 2D plane travels faster than the wave polarized within the 2D plane. On the other hand, when the seismic ray travels through a horizontally stretched melt such as in the lowermost ULVZ, $V_{S1} = V_{S2}$ and we do not observe anisotropy. When the melt is stretched in the intermediate direction such as in the both sides of the plume head, the S1-wave can be faster or slower than the S2 wave depending on the direction of the melt disk. As a consequence, we obtain a striped pattern of anisotropy, largest along the upwellings.

The second case is where the ray travels perpendicular to the calculated 2D plane, i.e., parallel to the axis of the assumed convective rolls. In this case, the ray path is always perpendicular to the symmetrical axis of the ellipsoids, and the magnitude of anisotropy is determined by the melt fraction and aspect ratio alone. From Figs. 2 and 3, we find that the anisotropy is always of $V_{S1} > V_{S2}$ type and its magnitude is large. As a result, when the seismic wave travels through a vertically stretched melt, S1 = SV, and S2 = SH, and vice versa when travelling through a horizontally stretched melt. Accordingly, the vertical profile would be strikingly different depending on the distance from the axis of the plume. A vertical profile of a ray passing through the axis of the plume would be always $V_{SV} > V_{SH}$ regardless of depth. A vertical profile of a ray passing slightly off-axis from the plume axis would be $V_{SH} > V_{SV}$ in the plume head, large $V_{SV} > V_{SH}$ anisotropy in the conduit and $V_{SH} > V_{SV}$ in the base of the plume. A vertical profile of a ray passing largely off-axis from the plume axis such that it does not pass through the conduit would be $V_{SV} > V_{SH}$ in the plume head, absence of anisotropy beneath it because of no melting, and $V_{SH} > V_{SV}$ at the base of the plume.

Our results can infer the validity of transversely isotropic approximation. From Fig. 8, we find that transverse isotropy with approximately vertical symmetry axis exists at base of the plume stem and in the upper most part of plume head, and those for horizontal symmetry axis at other parts of the the base of the mantle. Otherwise the melts are tilted and as a result, azimuthal anisotropy and SV–SH coupling would appear. The possibility of the azimuthal anisotropy under Pacific has been inferred by Maupin (1994). Recently, Garnero et al. (2004) found a SV–SH coupling and an alternating pattern of tilted transverse isotropy with a spatial scale of several hundred kilometers beneath the Carribean. One interpretation for this is that it is due to seismic waves travelling nearly parallel to the axis of convection rolls. A better azimuthal coverage of the D″-layer, like those which have been done for the inner core (Helffrich et al., 2002), would help to resolve such structure in the future.

4.3. Cases for other temperature parameters

In this paper, we have mainly discussed the calculation for the top temperature $T_u = 2200$ K and the solidus temperature $T_S = 3750$ K. We have also made calculations for other temperature parameters. Part of the results for other two top temperatures, 2000 and 1500 K, are already shown in Figs. 12 and 13.

Different top temperatures T_u leads to two noticeably different convection regimes. For $T_u \lesssim 2500$ K, which includes our main calculations with $T_u = 2200$ K, convection begins in a horizontal layer, whose depth scale gradually increases with time. Above the layer extends a low-temperature viscous fluid which is almost stagnant. We call this flow regime "the small-scale convection regime", following Solomatov and Moresi (2002). This regime approximately corresponds to the stagnant-lid asymptotic regime of Solomatov (1995). For $T_u \gtrsim 3000$ K, convection begins in the form of plumes.

Plumes penetrate into the low-temperature region above. We call this flow regime "the plume-dominant regime". This regime approximately corresponds to the small viscosity contrast regime of Solomatov (1995). The difference of the two regimes is most clearly seen at the beginning of convection. Whether the convection takes the form of convection cells or plumes is the main difference. Even in the small-scale convection regime, when the convection layer becomes thick enough after a long time, plumes form and penetrate into the viscous fluid above.

For plume-dominant regime, partial melting is confined to the lowermost 5 km, and the anisotropy forms only at the base. On the other hand, in the small-scale convection regime, melting occurs within the convection layer well above the lower thermal boundary layer, and a three layered anisotropic structure forms. The presence of anisotropy at upper part of D″ layer is generally reported in circum-Pacific regions (Lay et al., 1998a) which is often associated with cold downwellings. Since small-scale convection occurs for a relatively cold mantle, our results suggests that partial melting may also be the cause of anisotropy at these regions.

Note that the effect of increasing T_u (or decreasing T_b) has a similar effect as decreasing the activation energy, because the Frank-Kamenetskii parameter (8) decreases by both of these changes. This allows us to infer the effect of changing the activation energy, which has large uncertainties.

The effect of changing the solidus temperature T_S can easily be inferred from Figs. 4 and 5, because the melt is passive and does not affect the flow in our model. When $T_S \gtrsim 3850$ K, melting occurs almost only in the lowermost boundary layer (ULVZ), and seismic anisotropy appears almost only in the ULVZ. When $T_S \lesssim 3500$ K, melting occurs in the almost entire convective layer, which corresponds to the D″ layer. The melt fraction at the axis of a plume at 171.42 Myr increases from about 6% ($T_S = 3750$ K) to above 17% ($T_S = 3500$ K). The seismic anisotropy and velocity reduction increases accordingly.

4.4. Validity of two-dimensionality

Here we discuss the validity of two-dimensionality of the convection model we used. Three-dimensional convection calculations with a temperature-dependent viscosity by Ogawa et al. (1991) give us a clue to the problem. They showed that the convection pattern falls into two regimes. One is the whole-layer convection regime, where fluid flows even in the viscous upper boundary. This type of flow occurs when the viscosity contrast across the layer is small (i.e., small γ), and roughly corresponds to our plume-dominant regime. The other is the stagnant-lid regime, where the fluid near the upper boundary does not move due to large viscosity. This type of flow occurs when the viscosity contrast across the layer is large (i.e., large γ), and roughly corresponds to our small-scale convection regime. Ogawa et al. (1991) showed that the pattern of convection is three-dimensional in the stagnant-lid regime with rectangular convection cells. In the whole-layer convection regime, the convection pattern is two-dimensional rolls when the Rayleigh number is small, and becomes three-dimensional with rectangular cells when the Rayleigh number is more than one or two orders of magnitude above critical.

Thus, the problem is the correspondence between our calculations and theirs. The difference of the form of temperature dependence of viscosity makes it difficult for us to compare Ogawa et al. (1991)'s results and ours. Their temperature dependence has the exponential form, while ours is of the Arrhenius type. One idea is the use of the Frank-Kamenetskii parameter γ. Our value of γ is 7, which is less than 8, and this means that our calculation for $T_u = 2200$ K is in the range of the whole-layer convection regime of Ogawa et al. (1991). This suggests that the convection begins as two-dimensional rolls, and eventually becomes three-dimensional as the thickness of the convection layer increases. Hence our two-dimensional calculations would be valid. On the other hand, if we regard our small-scale convection regime as corresponding to their stagnant-lid regime, the convection will begin as three-dimensional rectangular cells, and the validity of our two-dimensional would be dubious.

It could be argued that the convection will begin in the form of two-dimensional rolls because the viscosity contrast within the convecting region is small. Temperature drops occur mainly in the boundary layers and the temperature within the convecting region is relatively uniform. If this argument is correct, we might use the regime diagram of Krishnamurti (1970) for uniform viscosity to infer the three-dimensional evolution of the convection pattern. If we take the thickness of the convective layer as 50 km, the temperature difference across the convecting layer as 600 K, and the mean viscosity as 5×10^{18} Pas we obtain $Ra \sim 7500$. This is in the regime of steady two-dimensional rolls for high Prandtl numbers, suggesting that the small-scale convection initially starts as two-dimensional rolls. Transformation to three-dimensional convection occurs when the thickness of the convecting layer exceeds about 70 km.

4.5. Effect of latent heat

In this section, we consider how latent heat, which are neglected in our model, would affect our results.

Latent heat buffers temperature changes. For example when melting occurs, latent heat is absorbed, and as a result, the increase in temperature and further melting are buffered. A similar argument applies for freezing. We can quantitatively evaluate this effect as follows. The energy equation including the latent heat is

$$\frac{\mathrm{D}T}{\mathrm{D}t} = \kappa\nabla\cdot\nabla T - \frac{L}{C_\mathrm{p}}\frac{\mathrm{D}\phi}{\mathrm{D}t}. \tag{15}$$

Here L is the latent heat per unit mass, and ϕ is the melt fraction. Assuming that ϕ is a linear function of temperature, we can rewrite the above equation as

$$\left(1 + \frac{L}{C_\mathrm{p}}\frac{\mathrm{d}\phi}{\mathrm{d}T}\right)\frac{\mathrm{D}T}{\mathrm{D}t} = \kappa\nabla\cdot\nabla T \tag{16}$$

Let us evaluate the second term of the left hand side β.

$$\beta = \frac{L}{C_\mathrm{p}}\frac{\mathrm{d}\phi}{\mathrm{d}T} \tag{17}$$

Latent heat is expressed as $L = T_\mathrm{m}\Delta S$, where T_m is the melting temperature, ΔS is the entropy of melting. For ΔS, we use the value for enstatite ($MgSiO_3$); $\Delta S \simeq 40$ J/mol/K (Richet and Bottinga, 1986). With the assumed melting temperature $T_\mathrm{m} = 3750$ K, we get $L = 1.5\times10^6$ J/kg. Using $\mathrm{d}T = 1750$ K as the temperature difference between the solidus and liquidus, we obtain $(\mathrm{d}\phi/\mathrm{d}T) \simeq 6\times10^{-4}$(1/K). Using $C_\mathrm{p} = 1200$ J/kg/K, we obtain $\beta \sim 0.75$. We can define an effective thermal diffusivity

$$\kappa_\mathrm{eff} = \frac{\kappa}{1+\beta} \tag{18}$$

and obtain $\kappa_\mathrm{eff} = 0.6\kappa$.

This result implies that the effective thermal diffusivity is reduced by about a factor of 2 and heating and cooling is slowered. Accordingly in the lowermost boundary layer where melting takes place, the resulting melt fraction would be reduced when latent heat is taken into account. We note, however, that the magnitude of the S-wave anisotropy is more sensitive to the aspect ratio of the inclusions than to the melt fraction, and even for a reduced melting, large deformation would yield large seismic anisotropy.

5. Conclusions

We modeled the deformation of a partially molten layer at the base of the mantle caused by small-scale convection. We found that for a set of possible parameter values for the mantle, partial melt can be strongly deformed and align preferentially as soon as the thermal instability occurs. Our model predicts a three-layer structure of seismic anisotropy in the D″ layer, if melting occurs not only in the ULVZ but extends to the top of hot regions of the D″ layer. We also showed that the alignment of melt inclusions is important in forming the seismological ULVZ. The fine-structures seen in our calculations can be tested using better azimuthal coverage of seismic ray paths.

Our model is intended to serve as a starting point to making more realistic model of the deformation of partial melt in the D″ layer. Note that our model has various limitations. For example, the results we showed are mainly for one set of T_S and T_u. Results for other parameters, which show diverse behaviors, are partly discussed in the text, but not fully investigated. Moreover, the assumptions of two-dimensionality and passive deformation of melt pockets are to be scrutinized in the future.

Acknowledgments

We thank O. Nishizawa and T. Yoshino for kindly providing the code to calculate the elastic constants of partial melt. We are grateful to A. Namiki, E. Garnero, A. McNamara and an anonymous reviewer for their helpful comments on the manuscript. Most of the figures used in this paper were drawn using GMT. Part of this work was supported by Grant-in-Aid for Scientific Research No.15740272, Japan Society for the Promotion of Science.

References

Boehler, R., 1996. Melting temperature of the Earth's mantle and core:Earth's thermal structure. Annu. Rev. Earth Planet. Sci. 24, 15–40.

Boehler, R., 2000. High-pressure experiments and the phase diagram of lower mantle and core materials. Rev. Geophys. 38, 221–245.

Chopelas, A., Boehler, R., 1989. Thermal expansion measurements at very high pressure, systematics, and a case for a chemically homogeneous mantle. Geophys. Res. Lett. 16, 1347–1350.

Christensen, U.R., 1984. Instability of a hot boundary layer and initiation of thermo-chemical plumes. Annal. Geophys. 2, 311–320.

Clauser, C., Kiesnar, S., 1987. A conservative, unconditionally stable, second-order three-point differencing scheme for the diffusion-convection equaation. Geophys. J. R. Astron. Soc. 91, 557–568.

Cooper, R.F., Kohlstedt, D.L., 1982. Interfacial energies in the olivine-basalt system. Adv. Earth Planet. Sci. 12, 217–228.

Cormier, V.F., 2000. D″ as a transition in the heterogeneity spectrum of the lowermost mantle. J. Geophys. Res. 105, 16193–16205.

Duffy, T., 2004. Deeper understanding. Nature 430, 409–410.

Dziewonski, A.M., Anderson, D.L., 1981. Preliminary reference Earth model. Phys. Earth Planet. Int. 25, 297–356.

Eshelby, J., 1957. The determination of the elastic field of an ellipsoidal inclusion, and related problems. Proc. R. Soc. London A241, 376–396.

Fouch, M.J., Fischer, K.M., Wysession, M.E., 2001. Lowermost mantle anisotropy beneath the Pacific: imaging the source of the Hawaiian plume. Earth Planet. Sci. Lett. 190, 167–180.

Frost, H.J., Ashby, M.F., 1982. Deformation-mechanism maps. Pergamon Press pp. 7–180.

Garnero, E.J., 2000. Heterogeneity of the lowermost mantle. Ann. Rev. Earth Planet Sci. 28, 509–537.

Garnero, E.J., Maupin, V., Lay, T., Fouch, M.J., 2004. Variable azimuthal anisotropy in Earth's lowermost mantle. Science 306, 259–261.

Helffrich, G., Kaneshima, S., Kendall, J.-M., 2002. A local, crossing-path study of attenuation and anisotropy of the inner core. Geophys. Res. Lett. 12, doi:10.1029/2001GL014059.

Hofmeister, A.M., 1999. Mantle values of thermal conductivity and the geotherm from phonon lifetimes. Science 283, 1699–1706.

Holtzman, B.K., Kohlstedt, D.L., Zimmerman, M.E., Heidelbach, F., Hiraga, T., Hustoft, J., 2003. Melt segregation and strain partitioning: implications for seismic anisotropy and mantle flow. Science 301, 1227–1230.

Iitaka, T., Hirose, K., Kawamura, K., Murakami, M., 2004. The elasticity of the $MgSiO_3$ post-perovskite phase in the Earth's lowermost mantle. Nature 430, 442–445.

Karato, S.-I., 1998. Seismic anisotropy in the deep mantle, boundary layers and the geometry of mantle convection. Pure Appl. Geophys. 151, 565–587.

Kendall, J.-M., Silver, P.G., 1996. Constraints from seismic anisotropy on the nature of the lowermost mantle. Nature 381, 409–412.

Kendall, J.-M., Silver, P.G., Investigating causes of D″ anisotropy, In: Gurnis, M., Wysession, M.E., Knittle, E., Buffett, B.A., (Eds.), The Core-Mantle Boundary Region, Geodynamics Series, vol. 28, Am. Geophys. Union, Washington DC, USA, 1998. pp. 97–118.

Kendall, J.-M., Seismic anisotropy in the boundary layers of the mantle, In: Karato, S.-I., Forte, A., Liebermann, R., Masters, G., Stixrude, L., (Eds.), Earth's Deep Interior: Mineral Physics and Tomography From the Atomic to the Global Scale, Geophysical Monograph, vol. 117, Am. Geophys. Union, Washington DC, USA, 2000. pp. 133–159.

Krishnamurti, R., 1970. On the transition to turbulent convection. J. Fluid Mech. 42, 295–320.

Lambeck, K., Johnston, P., Nakada, M., 1990. Holocene glacial rebound and sea-level change in NW Europe. Geophys. J. Int. 103, 451–468.

Lay, T., Williams, Q., Garnero, E.J., 1998. The core-mantle boundary layer and deep Earth dynamics. Nature 392, 461–468.

Lay, T., Williams, Q., Garnero, E.J., Kellogg, L., Wysession, M.E., Seismic wave anisotropy in the D″ region and its implications, In: Gurnis, M., Wysession, M.E., Knittle, E., Buffett, B.A., (Eds.), The Core-Mantle Boundary Region, Geodynamics Series, vol. 28, Am. Geophys. Union, Washington DC, USA, 1998. pp. 299–318.

Lay, T., Garnero, E.J., Williams, Q., 2004. Partial melting in a thermo-chemical boundary layer at the base of the mantle. Phys. Earth Planet. Int. 146, 441–467.

Maupin, V., 1994. On the possibility of anisotropy in the D″ layer as inferred from the polarization of diffracted S-Waves. Phys. Earth Planet. Int. 87, 1–32.

McKenzie, D., 1979. Finite deformation during fluid flow. Geophys. J. R. Astron. Soc. 58, 689–715.

McNamara, A.K., Karato, S.-I., van Keken, P.E., 2001. Localization of dislocation creep in the lower mantle: implications for the origin of seismic anisotropy. Earth Planet. Sci. Lett. 191, 85–99.

McNamara, A.K., van Keken, P.E., Karato, S.-I., 2002. Development of anisotropy structure in the Earth's lower mantle by solid-state convection. Nature 416, 310–314.

McNamara, A.K., van Keken, P.E., Karato, S.-I., 2003. Development of finite strain in the convecting lower mantle and its implications for seismic anisotropy. J. Geophys. Res. 108, doi:10.1029/2002JB001970.

Murakami, M., Hirose, K., Kawamura, K., Sata, N., Ohishi, Y., 2004. Post-perovskite phase transition in $MgSiO_3$. Science 304, 855–858.

Musgrave, M.J.P., 1970. Crystal Acoustics: introduction to the study of elastic waves and vibrations in crystals. Holden-Day, San Francisco 406pp.

Nakakuki, T., Sato, H., Fujimoto, H., 1994. Interaction of the upwelling plume with the phase and chemical boundary at the 670 km discontinuity: effects of temperature-dependent viscosity. Earth Planet. Sci. Lett. 121, 369–384.

Navrotsky, A., Thermodynamic properties of minerals, In: Ahrens, T.J., (Ed.), Mineral Physics and Crystallography: A Handbook of Physical Constants, AGU Reference Shelf, vol. 2, Am. Geophys. Union, Washington DC, USA, 1995. pp. 18–28.

Nishizawa, O., 1982. Seismic velocity anisotropy in a medium containing oriented cracks - transversely anisotropic case. J. Phys. Earth 30, 331–347.

Nishizawa, O., Yoshino, T., 2001. Seismic velocity anisotropy in mica-rich rocks: an inclusion model. Geophys. J. Int. 145, 19–32.

Oganov, A.R., Ono, S., 2004. Theoretical and experimental evidence for a post-perovskite phase of $MgSiO_3$ in Earth's D″ layer. Nature 430, 445–448.

Ogawa, M., Schubert, G., Zebib, A., 1991. Numerical simulations of three-dimensional thermal convection in a fluid with strongly temperature-dependent viscosity. J. Fluid Mech. 233, 299–328.

Olson, P., Schubert, G., Anderson, C., 1987. Plume formation in the D″-layer and the roughness of the core-mantle boundary. Nature 327, 409–413.

Panning, M., Romanowicz, B., 2004. Inferences on Flow at the Base of Earth's Mantle based on seismic anisotropy. Science 303, 351–353.

Pulliam, J., Sen, M.K., 1998. Seismic anisotropy in the core-mantle transition zone. Geophys. J. Int. 135, 113–128.

Revenaugh, J., Meyer, R., 1997. Seismic evidence of partial melt within a possibly ubiquitous low-velocity layer at the base of the mantle. Science 277, 670–673.

Richet, P., Bottinga, Y., 1986. Thermochemical properties of silicate glasses and liquids. Rev. Geophys. 24, 1–25.

Ritsema, J., Garnero, E., Lay, T., 1997. A strongly negative shear velocity gradient and lateral variability in the lowermost mantle beneath the Pacific. J. Geophys. Res. 102, 20395–20411.

Ritsema, J., Lay, T., Garnero, E.J., Benz, H., 1998. Seismic anisotropy in the lowermost mantle beneath the Pacific. Geophys. Res. Lett. 25, 1229–1232.

Russell, S.A., Lay, T., Garnero, E.J., 1998. Seismic evidence for small-scale dynamics in the lowermost mantle at the root of the Hawaiian hotspot. Nature 396, 255–258.

Russell, S.A., Lay, T., Garnero, E.J., 1999. Small-scale lateral shear velocity and anisotropy heterogeneity near the core-mantle boundary beneath the central Pacific imaged using broadband ScS waves. J. Geophys. Res. 104, 13183–13199.

Schott, B., Yuen, D.A., Braun, A., 2002. The influence of composition and temperature-dependent rheology in thermo-chemical convec-

tion on entrainment of the D″-layer. Phys. Earth Planet. Int. 129, 43–65.

Schubert, G., Turcotte, D.L., Olson, P., 2001. Mantle Convection in the Earth and Planets. Cambridge Univ. Press, Cambridge 940 pp.

Sidorin, I., Gurnis, M., Geodynamically consistent seismic velocity predictions at the base of the mantle, In: Gurnis, M., Wysession, M.E., Knittle, E., Buffett, B.A., (Eds.), The Core-Mantle Boundary Region, Geodynamics Series, vol. 28, Am. Geophys. Union, Washington DC, USA, 1998. pp. 209–230.

Sidorin, I., Gurnis, M., Helmberger, D.V., Ding, X., 1998. Interpreting D″ seismic structure using synthetic computed from dynamic models. Earth Planet. Sci. Lett. 163, 31–41.

Sidorin, I., Gurnis, M., Helmberger, D.V., 1999. Dynamics of a phase change at the base of the mantle consistent with seismological observations. J. Geophys. Res. 104, 15005–15023.

Singh, S.C., Taylor, M.A., Montagner, J.P., 2000. On the presence of liquid in Earth's inner core. Science 287, 2471–2474.

Solomatov, V.S., 1995. Scalling of temperature- and stress-dependent viscosity convection. Phys. Fluids 7, 266–274.

Solomatov, V.S., Moresi, L.N., 2002. Small-scale convection in the D″ layer. J. Geophys. Res. 107, doi:10.1029/2000JB000063.

Stengel, K.C., Oliver, D.S., Booker, J.R., 1982. Onset of convection in a variable-viscosity fluid. J. Fluid Mech. 120, 411–431.

Taylor, M.A.J., Singh, S.C., 2002. Composition and microstructure of magma bodies from effective medium theory. Geophys. J. Int. 149, 15–21.

Thomas, C., Weber, M., Agnon, A., Hofstetter, A., 1998. A low-velocity lamella in D″. Geophys. Res. Lett. 25, 2885–2888.

Thompson, P.F., Tackley, P.J., 1998. Generation of mega-plumes from the core-mantle boundary in a compressible mantle with temperature-dependent viscosity. Geophys. Res. Lett. 25, 1999–2002.

Vinnik, L., Romanowicz, B., Lestunff, Y., Makeyeva, L., 1995. Seismic anisotropy in the D″ layer. Geophys. Res. Lett. 22, 1657–1660.

Williams, Q., Garnero, E.J., 1996. Seismic Evidence for partial melt at the base of Earth's mantle. Science 273, 1528–1530.

Yamazaki, D., Karato, S.-I., 2001. Some mineral physics constraints on the rheology and geothermal structure of Earth's lower mantle. Am. Mineral. 86, 385–391.

Zerr, A., Diegeler, A., Boehler, R., 1998. Solidus of Earth's deep mantle. Science 281, 243–246.

Zhang, S., Zimmerman, M.E., Daines, M.J., Karato, S.-i., Kohlstedt, D.L., 1995. Lattice preferred orientation and melt distribution in experimentally sheared olivine-basalt rocks. EOS, Trans. AGU 75, S281.

Zimmerman, M.E., Zhang, S., Kohlstedt, D.L., 1999. Melt distribution in mantle rocks deformed in shear. Geophys. Res. Lett. 26, 1505–1508.